npj computational materials

www.nature.com/npjcompumats

ARTICLE OPEN

Check for updates

Physics guided heat source for quantitative prediction of IN718 laser additive manufacturing processes

Abdullah Al Amin[1,2]✉, Yangfan Li[1], Ye Lu[3], Xiaoyu Xie[1], Zhengtao Gan[4], Satyajit Mojumder[5], Gregory J. Wagner[1] and Wing Kam Liu[1]✉

Challenge 3 of the 2022 NIST additive manufacturing benchmark (AM Bench) experiments asked modelers to submit predictions for solid cooling rate, liquid cooling rate, time above melt, and melt pool geometry for single and multiple track laser powder bed fusion process using moving lasers. An in-house developed **A**dditive **M**anufacturing **C**omputational **F**luid **D**ynamics code (AM-CFD) combined with a cylindrical heat source is implemented to accurately predict these experiments. Heuristic heat source calibration is proposed relating volumetric energy density (ψ) based on experiments available in the literature. The parameters of the heat source of the computational model are initially calibrated based on a Higher Order Proper Generalized Decomposition- (HOPGD) based surrogate model. The prediction using the calibrated heat source agrees quantitatively with NIST measurements for different process conditions (laser spot diameter, laser power, and scan speed). A scaling law based on keyhole formation is also utilized in calibrating the parameters of the cylindrical heat source and predicting the challenge experiments. In addition, an improvement on the heat source model is proposed to relate the Volumetric Energy Density (VED_σ) to the melt pool aspect ratio. The model shows further improvement in the prediction of the experimental measurements for the melt pool, including cases at higher VED_σ. Overall, it is concluded that the appropriate selection of laser heat source parameterization scheme along with the heat source model is crucial in the accurate prediction of melt pool geometry and thermal measurements while bypassing the expensive computational simulations that consider increased physics equations.

npj Computational Materials (2024)10:37 ; https://doi.org/10.1038/s41524-024-01198-6

INTRODUCTION

Additive manufacturing (AM) processes such as laser powder bed fusion (LPBF), selective laser melting (SLM), and directed energy deposition (DED) for metal alloys enable the production of complex, lightweight parts at reduced manufacturing costs[1–5]. Though AM is a promising manufacturing technology, it is facing numerous challenges in printed part qualification and certification in aerospace, automotive, and biomedical engineering applications. Inherent process variabilities and uncertainties in processing parameters (e.g., laser scan speed, power, and spot diameter) lead to numerous manufacturing defects such as cracking[6], porosity[7,8], roughness[9,10], balling[11], inclusion[12], and bead-up[13]. Combined efforts from academia, industry, and government organizations sought to fully realize the potential of AM technology through a better understanding of the process-structure-performance of the AM materials systems. On this aspect, the National Institute of Standards and Technology (NIST) and Air Force Research Laboratory (AFRL) led the efforts from government organizations by arranging several benchmark challenges in 2018[14], 2020[15], and 2022[16], respectively. Through these efforts, they developed state-of-the-art experimental facilities for AM technologies and organized several benchmark challenges for modelers to develop predictive simulations of experimental measurements. These predictive modeling and simulation tools are critical considering the experimental cost and efforts required for the AM-built part qualification and certification. Hence, this article focuses on the NIST AM Bench 2022 Challenge 3 experiments organized by NIST and demonstrates methods to quantitatively model and predict different measurements. These experiments were performed for the LPBF AM process, where processing conditions such as laser power, scan speed, and spot diameter settings are varied for stationary and moving lasers in single and multi-track setups.

AM Bench 2022 Challenge 3 was designed to explore the effect of a wide range of laser parameters (power, scan speed, and spot diameter) for single and multi-track (pad) printing of the IN718 base plate. The melt pool behaviors for the variation of the processing conditions were reported using an in-situ process monitoring system[17–19] developed by NIST for location-specific liquid and solid cooling rates and the time above the melting temperature. Ex-situ measurements were performed to determine the after-printed geometry and microstructures. All these challenge experiments were blind predictions for the modelers, where the experimental results were revealed after the submission of the modeling results.

In recent years, numerous approaches for the AM process modeling have been proposed, varying the model's complexity from simple heat conduction to a complicated thermal-fluid model. The usual physics-based model requires extensive computational effort to reasonably solve the problem considering the AM process's inherent length and time scale[20,21]. The simplest of these modeling approaches was to consider the heat conduction equation[22,23]. However, the limitations of only using the heat conduction equations are that they cannot capture the interactions happening within the melt pool. Researchers have introduced equivalent heat conduction coefficients[24] to account for such discrepancy arising from missing physical interactions

[1]Department of Mechanical Engineering, Northwestern University, Evanston 60208 IL, USA. [2]Department of Mechanical and Aerospace Engineering, University of Dayton, Dayton, OH, USA. [3]Department of Mechanical Engineering, University of Maryland, Baltimore County, Baltimore, MD 21250, USA. [4]Department of Aerospace & Mechanical Engineering, University of Texas at El Paso, El Paso, TX, USA. [5]Theoritical and Applied Mechanics Program, Northwestern University, Evanston 60208 IL, USA. ✉email: aamin1@udayton.edu; w-liu@northwestern.edu

within the melt pool as modeled by Marangoni Convection and thermal-fluid vaporization model. Compared to this simplified model, consideration of thermal-fluid interaction improves the melt pool prediction, as demonstrated by Robichaud et al.[25]. It is understood that the primary driving force for convection was Marangoni flow which results in both inward and outward[26] flow at the surface of the melt pool. Neglecting this Marangoni flow leads to an overestimation of the melt pool depth. Therefore, it is necessary to consider Marangoni flow to obtain a reasonable estimation of melt pool depth and width. In addition to melt pool geometry, the solid and liquid cooling rates are important elements in carrying out the grain simulations. In addition to Marangoni flow, it is found that the consideration of thermal-fluid vaporization model is key in accurate prediction of the cooling rates[27]. Ignoring vaporization in the model also results in an overestimation of width. For cases of higher volumetric energy density, the phenomena are driven mostly by keyhole[28] formation, where other physical interactions, including surface evolution, dynamic change of heat input from the laser, and vaporization-driven recoil pressure, were important. The dynamic change in the heat input to the system was the most significant factor that dramatically affected the size and shape of the melt pool. In addition, the intensity of the laser attenuates as the laser travels through the keyhole plume, which can be captured through Beer-Lambert law[29,30]. Ignoring these physical interactions results in a non-physical rise in melt pool temperature, eventually affecting the solidification and cooling rate predictions for the high energy density cases.

Accurately predicting the cooling rates in the melt pool required capturing the necessary heat transfer phenomena, including convective and radiative heat transfer, in combination with the appropriate laser heat source. Furthermore, when the formation of the keyhole was not considered, the lack of vaporization physics in the model can lead to severe over-prediction of the cooling (both liquid and solid) rates. In addition to considering these crucial phenomena, the appropriate temperature-dependent material property also played a vital role in accurately predicting the experiment. It was expected that considering all these physics in a general sense should increase the fidelity of the prediction; however, at part-scale simulations, the analysis became expensive and difficult to manage within reasonable computational resources and time. This opened a new avenue to investigate different model reduction techniques and calibration schemes to approximate multiple physical field interactions into a simple form.

In an LPBF process, continuous melting, and remelting, including keyhole formation, were the underlying mechanism for part manufacturing. The quality of the printed parts mainly depended on the variation of this process. High-fidelity prediction of the quantification and qualification of AM parts mostly relied on accurately predicting the dimensions and dynamics of the melt pool. However, high accuracy prediction of the melt pool dynamics was challenging either because of the limitation of computational hardware required for the consideration of the increased number of physics fields or the process uncertainties involved in the AM process. Thus, relying mostly on the increased number of physics fields to improve the prediction accuracy of the melt pool dynamics was generally unsuccessful. Calibration of the heat source was one way to address this challenge, where a representative heating model was introduced in place of detailed laser heating models involving multiple reflections and ray tracing. Even in these scenarios, because of the highly variable processing conditions and uncertain non-linear material properties, these methods showed limited success in predicting melt pool dynamics. Recently, Lu et al. used a reduced order modeling technique[31] for efficient thermal-fluid coupled predictions and used a data-driven **H**igher-**O**rder **P**roper **G**eneralized **D**ecomposition (HOPGD)[32,33], to calibrate the process parameters for heat source models. In the present work, two different heat source models are proposed based on experimental observation. The first heat source is established based on a recent study of keyhole scaling law[34] during a laser powder bed fusion process and is titled scaling law-based heat source. The second heat source developed based on melt pool measurements correlating volumetric energy density (VED_σ) is titled physics-guided heat source model. Furthermore, using a finite volume-based thermal CFD (the AM-CFD)[27] model, the effort was extended to accurately capture the laser and melt-pool interaction for various NIST processing conditions.

The paper is organized as follows. In section 2, a summary of the NIST experiment is provided. The modeling methodology is introduced in Section 3 with the calibration methodology and materials properties. Section 4 compares predicted results for the different challenges of the AM Bench problem and discusses the limitation of the current modeling approach to accurately predict the experiment. Finally, Section 5 concludes by summarizing the current findings and referring to possible future extensions to the present model.

RESULTS AND DISCUSSION

The NIST single-track experiment is conducted on seven different laser processing conditions. The laser processing conditions are varied by laser power, scan speed, and spot diameter, as given in Table 1.

Model calibration with melt pool

Simplifying the heat source with a cylindrical model significantly reduces the computational effort as the problem Degrees of Freedom (DOF) is reduced by not considering multiphase field equations to capture interface change. When a cylindrical heat source is being used, it obviates the need to implement ray tracing in addition to surface evolution. Thus, the DOF is reduced by limiting the number of equations solved. However, one essential step of this cylindrical heat source method is calibrating the heat source for the given laser process conditions. The initial heat source calibration used available literature data for IN718[13,35–39]. The initial parameter space was generated from a preliminary simulation using the AM-CFD code. Based on the available simulation data, a HOPGD-based surrogate model was built to predict and optimize the heat source parameters for melt pool geometry prediction[31,40]. By comparing the surrogate model with the literature data, we calibrated the heat source parameters. Figure 1 compares the HOPGD prediction based on the "heuristic heat source parameterization" for the melt pool width and depth against the literature data. The calibration was made against the Balbaa et al.[35] measurements. Melt pool width and depth from other literature are presented as a comparison. Therefore, it is expected that the HOPGD prediction will have large difference

Table 1. Summary of the laser process conditions.

	Case number	Laser power (W)	Scan speed (mm s^{-1})	Spot size (μm)	VEDσ (J mm^{-3})	VED/VED_{base}
Baseline	0	285	960	67	1058	1
Change spot	1.1	285	960	49	1978	1.87
	1.2	285	960	82	706	0.67
Change speed	2.1	285	1200	67	847	0.8
	2.2	285	800	67	1270	1.2
Change power	3.1	325	960	67	1207	1.14
	3.2	245	960	67	910	0.86

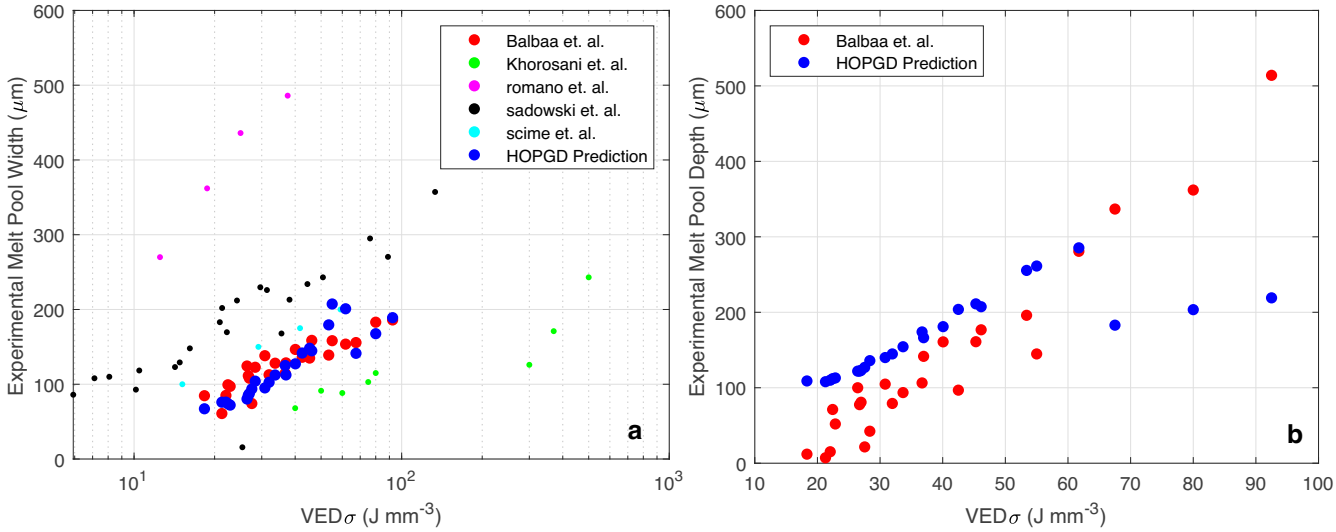

Fig. 1 Calibrating the parameters of heat source based on literature data for IN718. The parameters are calibrated against Balbaa et al.[35] Other literature data ((**a**) melt pool width, (**b**) melt pool depth) are presented for comparison.

when compared with other datasets. At lower volumetric energy density (VED) (below 70 J mm^{-3}), the melt pool width and depth both seem to agree well with the available literature data. One critical observation is that the depth prediction deviates from the experiment at a relatively lower VED compared to the width prediction. This was attributed to the fact that it was challenging to get the depth of the melt pool at higher VED_σ without the appropriate heat source model and interacting physics considering the surface evolution and multiple laser ray reflection. The reason for such a significant difference was that at higher VED_σ, the vapor depression layer or the keyhole layer depth starts to increase[41], and the heating of the base alloy becomes more complex, which was difficult to approximate with a simple cylindrical heat source model. As a result, the prediction at higher VED started to underestimate the system's heat input, resulting in smaller melt pool dimensions.

Prediction of solid cooling rates

The steps and process for experimental measurements of the solid cooling rates are summarized in supplementary method 6, details of which are available in[16]. Although experiments were performed on a plate of 1″ × 1″ dimension and the scan track length was 10 mm long, the computational prediction can be carried out on a much smaller domain (Supplementary Methods 3). This was because the steady state for melt pool evolution was reached much earlier (~3 ms) for all the processing conditions summarized in Table 1. Therefore, a preliminary computational analysis was carried out on the smallest and largest VED corresponding to cases 1.2 and 1.1, respectively (Table 1). This study was carried out to determine the minimum scan track length required to run the simulation to save computational time and computational resources. The original NIST experiments for single track were carried out on a track length of 10 mm. However, all the individual simulation cases were run in a reduced computational domain as determined by the length and time required to reach a steady state melt pool geometry. This is important for the accurate measurement of the temperature evolution and subsequently the cooling rates as well as melt pool depth and width measurements. Thus, the melt pool length was plotted for all the process conditions to confirm the attainment of a steady state for the measurements. Figure 2 demonstrates the process to estimate the time required to reach a steady state for the highest VED_σ case (case 1.1) was within ~3 ms and ~1 ms for the lowest VED_σ (case 1.2) cases. At this time, the laser travels ~2.9 mm and ~1.0 mm from the start location for case 1.1 and case 1.2, respectively. For both of these cases, 1.1 and 1.2, the scan speed was 960 mm s^{-1}. For all the other cases, the steady-state melt pool dimension was reached between these two times (~3 ms and ~1 ms). Thus, it was clear that the distance traveled was significantly smaller than the 10 mm domain length and facilitated reduced domain computation. Reducing the domain size significantly helped accelerate the computational simulation resulting in faster iteration and estimation of all the required measurements. The solid cooling rate was estimated from the slope of a linear fit over a temperature range starting from solidus temperature (1260 °C) and ending at 1150 °C. The same methodologies are followed to estimate the solid cooling rate from the simulation temperature data. Based on the first calibration scheme, the measurements of the solid cooling rates were plotted in Fig. 3 against changing VED_σ. It was observed from the results that the case at higher VED_σ overestimates the solid cooling rate. This was because the calibration scheme deposited much higher energy to the system to maintain the desired melt pool dimensions. This difference stemmed from the fact that there was heat loss from the vaporization and changing interface due to the formation of the keyhole. In the cylindrical heuristic heat source parameterization, no formation of a keyhole was considered, and thus the scheme resulted in a higher estimate of the peak temperature, increasing the estimate for solid cooling rate significantly. In comparison, the scaling law-based calibration has some form of keyhole generation and comes close to the solid cooling rate estimation, although slightly underestimating. However, in the physics-guided scheme, the heat source depth had a different correlation and resulted in a much more comparable estimate of the liquid cooling rate along with the solid cooling rate.

Prediction of liquid cooling rate

The liquid cooling rate was estimated at a temperature range from 1400 °C to a liquidus temperature of 1336 °C. The equation and methods used are similar to the solid cooling rate estimation and also use the slope of a linear fit to identify the liquid cooling rate, details of which were discussed by NIST in the challenge description[16]. A similar trend was also observed in the prediction of liquid cooling rate. The prediction of liquid cooling rate at lower VED was relatively in better agreement than at higher VED. The underlying cause was similar to what was explained before. The overestimation of the cooling rate comes from the non-physical

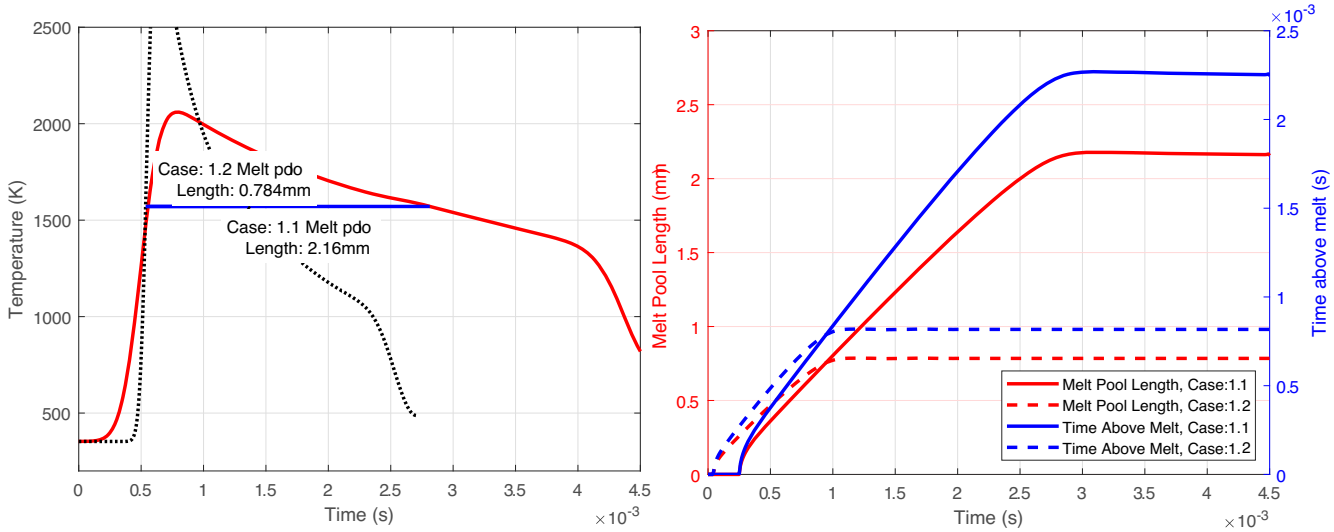

Fig. 2 Variation in time required to reach steady state for the lowest (case-1.1) and highest (case1.2) VED laser processing conditions.

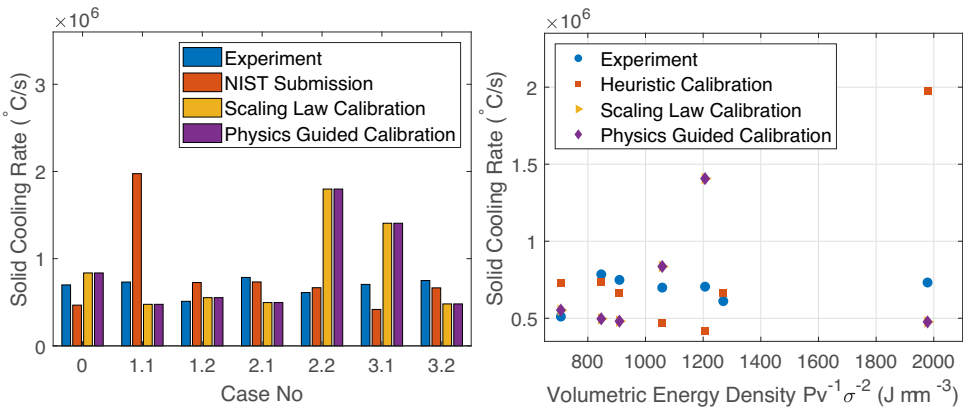

Fig. 3 Prediction of solid cooling rate against the volumetric energy density for IN718.

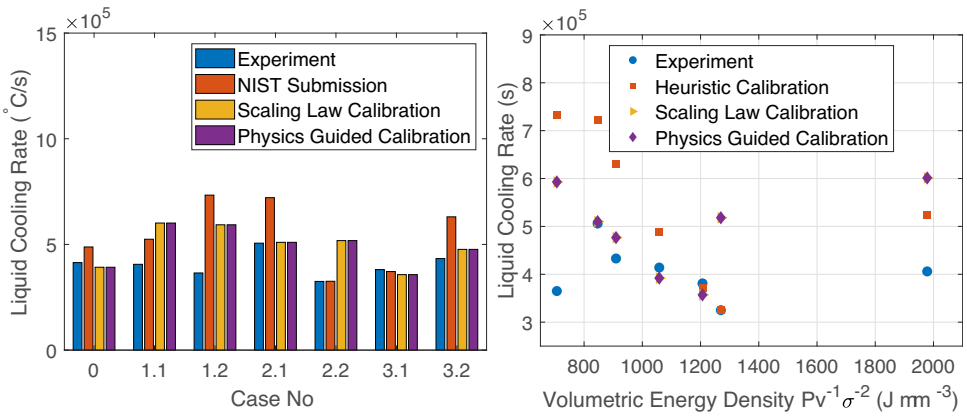

Fig. 4 Prediction of liquid cooling rate for the NIST AMB2022 challenge 03 experiment.

peak temperature, which was higher compared to the ambient, as the amount of heat input to the system was considerably higher than the actual scenario. The scaling law-based calibration scheme, as expected, overestimated the liquid cooling rate as the formation of the keyhole was absent at lower VED. Compared to the heuristic heat source parameterization, the updated physics-guided scheme showed improvement in predicting the liquid cooling rate, as shown in Fig. 4.

However, the scheme has its own limitation, which is more evident in case 2.2.

Prediction of time above melting

The time above melting was experimentally measured from in situ thermography data as the time spent above the midpoint between the liquidus and solidus temperature (1298 °C). Details

of how this time is measured are also elaborated in the NIST AM Bench challenge description[16]. Computationally, the measurement was performed on the same single-track analysis after the melt pool reached a steady state. During the steady state, the temperature distribution at the mid-point of the geometry was plotted against the track length. The track distance can then be mapped against time for a corresponding laser scan speed, and subsequently, the temperature vs. time plot was generated, as shown in Fig. 5. From the figure, the main characteristics of the plots for all the process conditions were observed to be similar. The total time above 1298 °C was measured from this plot and reported as track time above melt (TTAM). The comparison of simulated and experimental TTAM values is shown in Fig. 6. Unlike the solid and liquid cooling rates, the difference in TTAM between

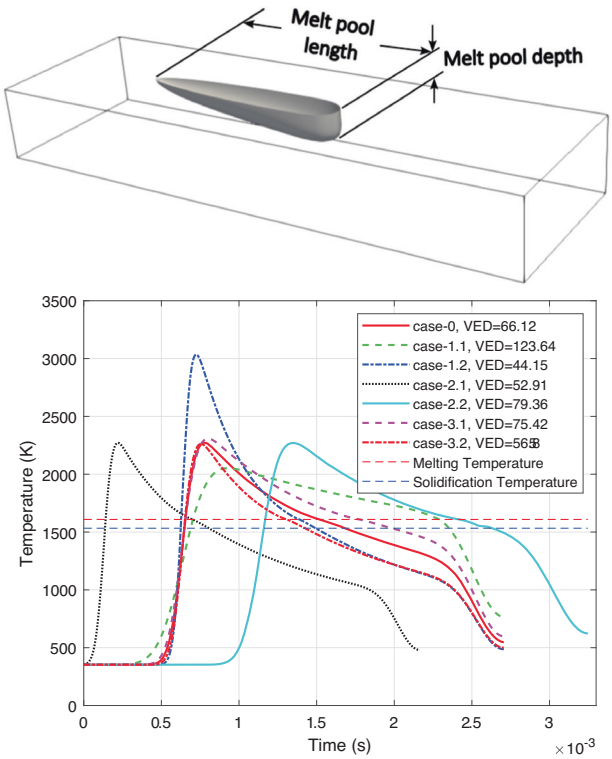

Fig. 5 Estimation of the time above melting for different volumetric energy density for IN718. The iso contour at the top is defined at liquidus temperature to represent the melt pool geometry.

prediction and experiment was minor. This is because the heat source was calibrated against the melt pool dimension, and the time above melting correlates with the melt pool dimensions. However, with the physics-guided heat source parameterization, the predictions improve, and the difference falls below 20% compared to the experiment.

Prediction of melt pool geometry

The prediction of melt pool geometry has the most accurate comparison with the experiment as the calibration was made against the melt pool dimensions. The physics-guided calibration further improves upon the prediction, bringing the prediction within 5% of the experimentally reported values (Figs. 7, 8). Not surprisingly, the melt pool dimensions for the higher VED cases also agree well with the experiments for both calibration schemes. The trend for melt pool dimension with respect to the VED was monotonically increasing as a result of increasing energy input going into the system. It is also interesting to compare the melt pool aspect ratio with the VED. It appears that the heuristic and scaling law-based calibration has limitations in predicting the aspect ratio. In this sense, the physics-guided calibration scheme that is developed based on the relationship to the aspect ratio rather than the melt pool width yields improved prediction, as evidenced in Fig. 9. The comparison of individual melt pool geometry for the seven different process conditions were compared in Fig. 10. It is also important and insightful to look at the relative errors of all the measurements for all the process conditions. Thus, a comparison table (Table 2) is provided comparing all the measurements for the three different heat source calibration schemes used in this study. From the table of relative error, it is observed that the physics-guided heat source performs well in most of the measurements, particularly the melt pool dimensions, specifically when compared with the heuristic and scaling law-based heat source. The heuristic calibration approach has noticeable disagreements with experimental measurements for the highest VED cases. This can be attributed to the inefficiency of the heat source model calibration in approximating the energy input to the system. In comparison, other heat source calibration schemes more accurately approximate the heat distribution to the system as the VED changes. As a result, the improvement in prediction of cooling rates and melt pool geometries are observed.

Prediction of Pad cooling rate, time above melt, and melt pool geometry

The steps to measure the cross-section was explained in the NIST challenge 3 result description document[16]. The location for which the measurements were made is shown in Fig. 11. The trend is

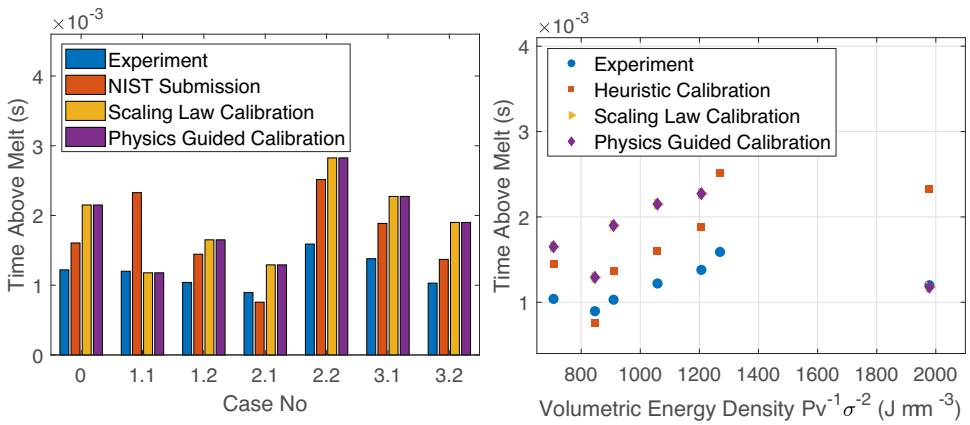

Fig. 6 Comparison of track time above melting for different laser process conditions.

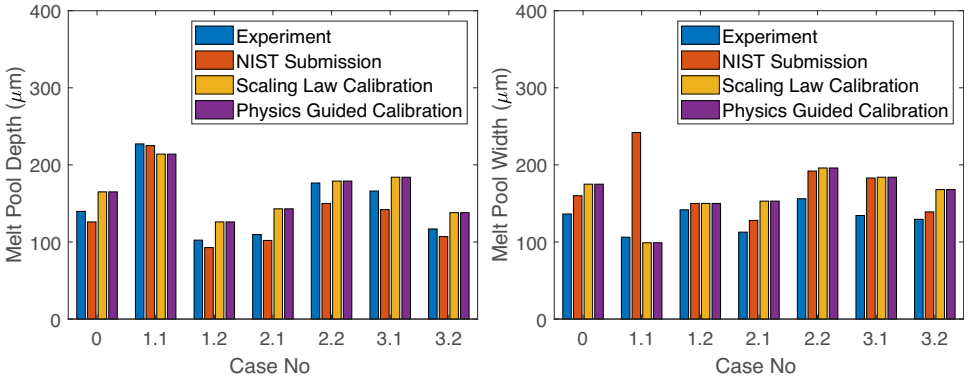

Fig. 7 Melt pool geometry measurements for the seven different process conditions.

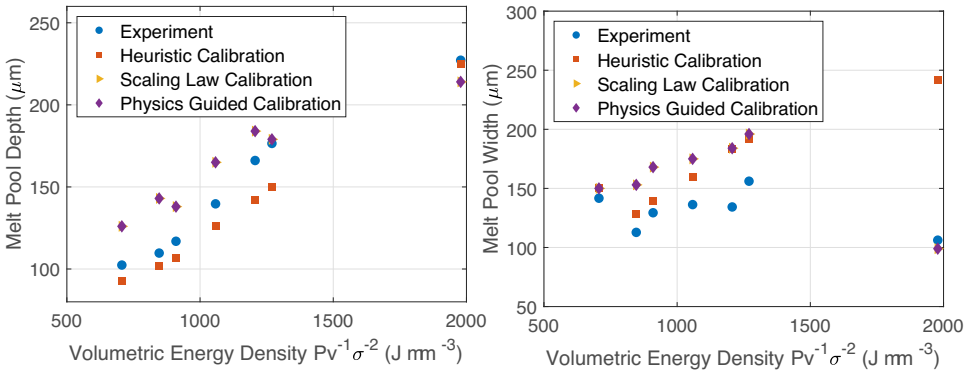

Fig. 8 Melt pool geometry comparison with VED. Although a linear correlation is apparent between melt pool depth and volumetric energy density, the relationship breaks apart when compared with melt pool width.

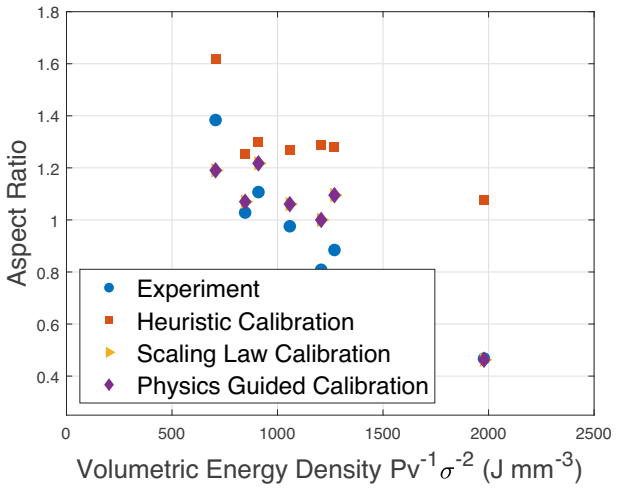

Fig. 9 The experimental measurements of the melt pool geometry has a linear trend with changing volumetric energy density. The heuristic calibration scheme failed to pick up the relationship whereas the physics informed calibration scheme shows improvement in the prediction.

similar for both calibration schemes. Following a similar trend, the calibration schemes successfully predicted the melt pool measurements for the multi-track (pad) laser scanning, as shown in Fig. 12. Figure 11 presents the locations P2 and P3 from the build plates BP2 and BP3. NIST Challenge 3 asked modelers to predict the overlap height and width along with the melt pool depth and width. The solid cooling rate and time above melting were also asked by NIST to be reported for the multi-track cases and thus shown in Fig. 13.

Interestingly, although the numerical measurements of these quantities mainly agreed within 10% of the experiment, the qualitative comparison of the melt pool shape was different. This is partially attributed to the lack of surface evolution physics and its space-time evolution statistics that were not considered in this computational model. The physical laser heat source, which depends strongly on surface evolution, was simplified with the cylindrical heat source assumption, which in turn primarily defines the geometric shape of the melt pool cross-section. Another interesting observation was the alternating depth of the melt pool cross section for the Y-direction scan. There are two competing explanations as to why this was happening. The first explanation was that the melt pool evolution takes some time to get to a steady state, as explained in section “Results and Discussion”, and thus the melt pool depth was smaller than the odd tracks, where the melt pool depth was significantly larger than its even track counterpart. The other understanding was the presence of gas flow along the negative -Y direction during the process, which significantly affected the heating from the laser resulting in the difference in the melted track depth. Since the effect of gas flow rate was not considered in the model and the simulation results cannot capture the change in the melt pool depth even after the steady state melt pool evolution was considered in the model, it was hypothesized that the variation in melt pool depth stems from neglecting the effect of gas flow.

In summary, three different calibration schemes for cylindrical heat sources were used to predict the 2022 NIST AM Bench Challenge 3 problems for various measurements. It was observed that the initial calibration scheme (heuristic heat source parameterization) was limited in terms of prediction at higher VED.

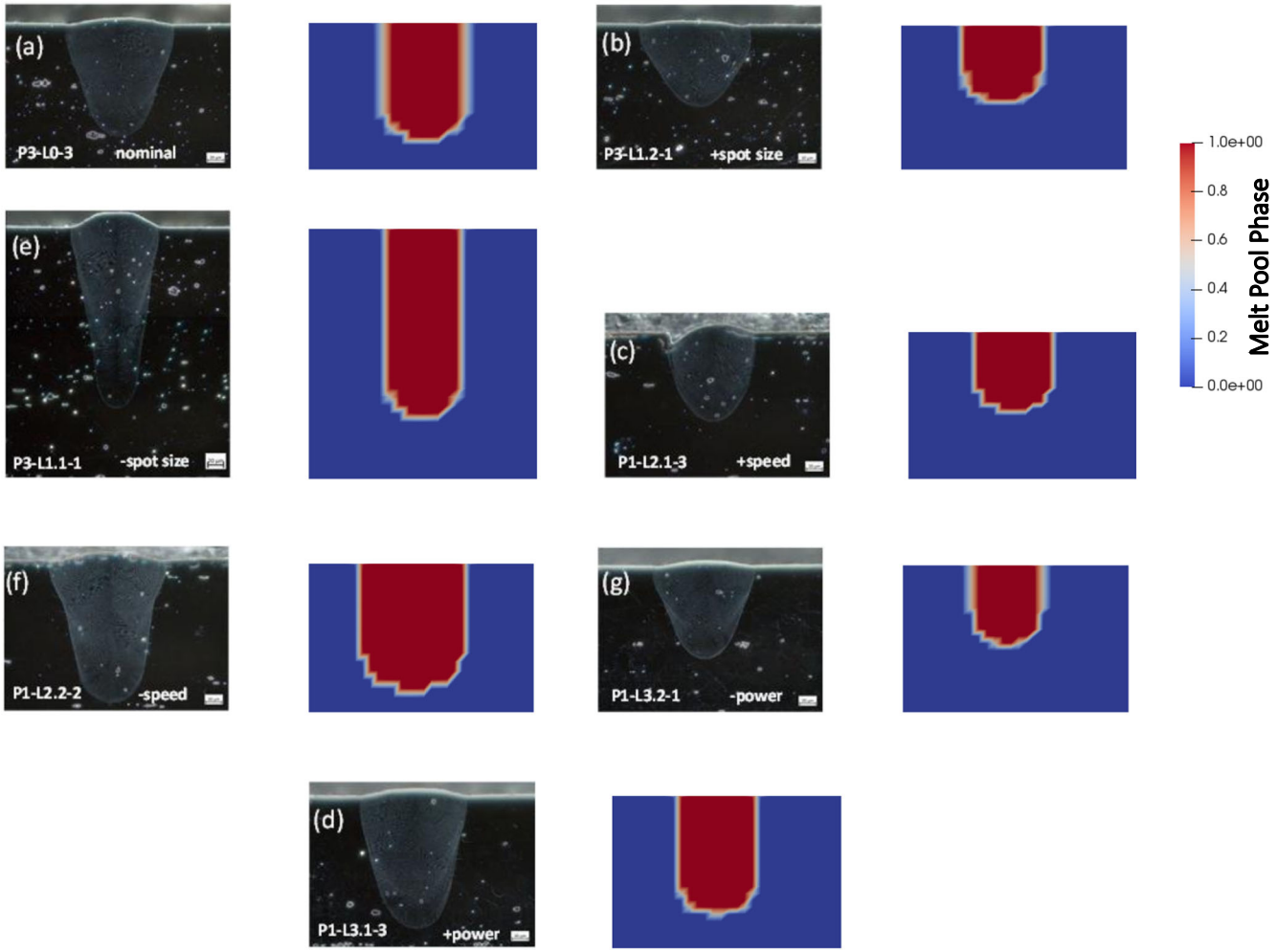

Fig. 10 Visual comparison of the melt pool geometry for the single-track scan laser experiment. a–f Correspond to cases detailed in Table 1 Case 0 to Case 3.2. The corresponding case ID is on the bottom left corner of the micrograph images.

Table 2. Summary of the relative error (in %) for simulations with experimental measurements.

		Case 0	Case 1.1	Case 1.2	Case 2.1	Case 2.2	Case 3.1	Case 3.2
Track time above melt	Heuristic	31.61	93.93	38.88	15.53	58.23	36.68	33.04
	Scaling	76.27	1.86	58.73	44.16	77.71	64.73	84.49
	Physics guided	15.80	2.88	29.79	24.11	46.06	12.00	22.32
Track solid cooling rate	Heuristic	33.16	169.81	42.16	6.63	9.16	40.74	11.19
	Scaling	19.62	34.91	8.19	36.75	194.32	99.48	35.77
	Physics guided	33.19	37.29	14.54	7.76	36.90	40.97	17.92
Track liquid cooling rate	Heuristic	17.86	29.22	100.90	42.54	0.22	2.46	45.62
	Scaling	5.30	48.08	62.43	0.78	59.40	6.29	10.08
	Physics guided	18.31	39.83	64.72	46.11	1.75	15.98	42.67
Track melt pool depth	Heuristic	9.81	0.97	9.47	7.02	15.01	14.51	8.47
	Scaling	18.11	5.81	23.05	30.36	1.42	10.78	18.05
	Physics guided	0.50	8.01	1.56	2.46	0.28	4.27	4.19
Track melt pool width	Heuristic	17.39	127.87	5.86	13.48	23.00	36.26	7.42
	Scaling	28.39	6.78	5.86	35.64	25.56	37.01	29.83
	Physics guided	2.42	0.75	1.62	1.06	2.50	2.76	3.40

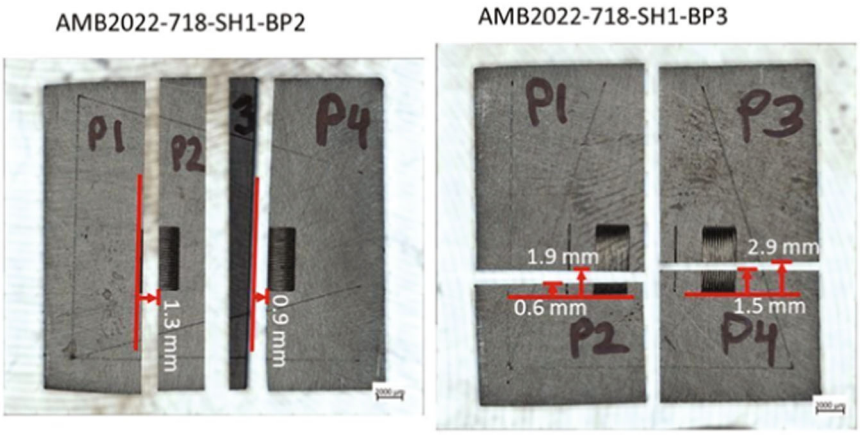

Fig. 11 Location of the multi-track scan where melted track measurements are made. Images are taken from the NIST 2022 AM Bench Challenge 3 experimental results[16].

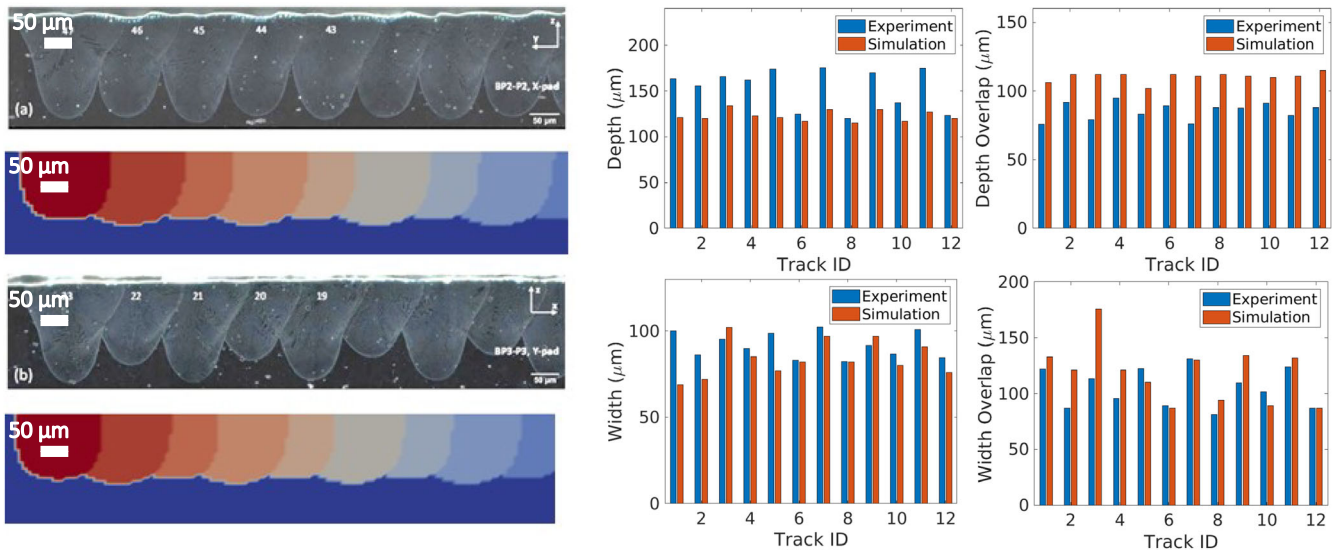

Fig. 12 Prediction of melt pool dimensions for the multi-track analysis for AMB2022-718-SH1-BP2 P2, and AMB2022-718-SH1-BP3 P3. **a** Represents the melted track when laser scan direction is across the gas flow and (**b**) represents the melted track when laser scan direction is along/against the gas flow direction.

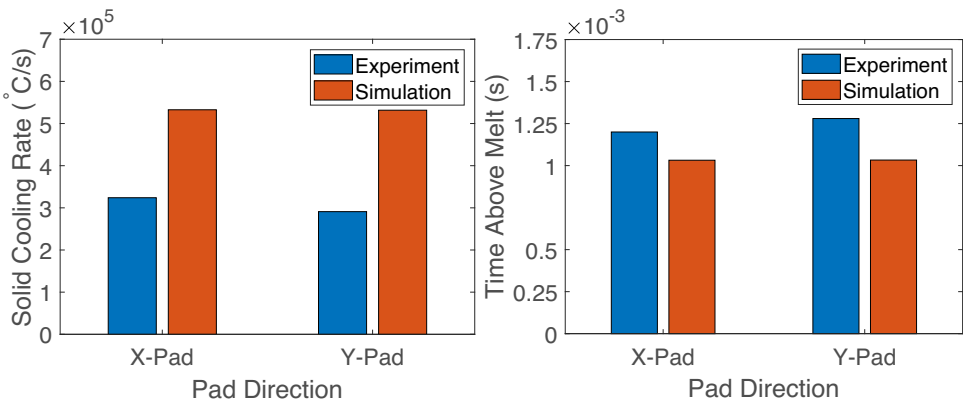

Fig. 13 Solid cooling rate and time above melting for the multi-track laser scan.

To improve the prediction accuracy, the heat source calibration scheme for melt pool width can be related to the melt pool geometries in a non-linear fashion to the VED_σ, improving the prediction significantly. It is understood that ignoring some essential physical interaction between the laser reflection, absorption, and diffusion through the vaporized metal/alloy gas can overestimate approximately 100% the cooling rates and time above melting. Thus, the refined approximate model (physics-guided heat source parameterization) based on experimental observation was established. Although the melt pool dimension (width and depth) predictions for multi-track simulation agreed well for such a calibration scheme, the melt pool's morphology was different where the melt pool overlap (depth and width) differed by approximately 55% due to the exclusion of the detailed surface evolution physics which is computationally time-consuming. However, the proposed prediction schemes that aim to approach part scale (multi-track and multi-layer) LPBF simulations approximating the laser heat source with the consideration of limited but fundamental physics equations yield reasonable accuracy in predicting the NIST AM Bench experiments.

METHODS

NIST experimental methods

Challenge 3 of the NIST AM Bench experiment involved IN718, and the objective of the test was the exploration of melt pool behaviors for individual single tracks and an overlapping 2D array of multi-tracks for different laser process conditions. The laser parameters (power, speed, and spot diameter) were varied for single-track experiments and kept at the base setting for the multi-track experiments. Two types of measurements, in-situ and ex-situ were carried out. In-situ measurements included time-resolved laser coupling, liquid and solid cooling rate, and location-specific time above melting; prediction of the last two was part of the challenge. Ex-situ measurements included 3D topography of the solidified laser track's cross-sectional geometry and micro-structural measurements. Only the melt pool measurements from the cross-section geometry were part of the challenge. The sample substrate of IN718 was cut from a rolled and annealed sheet and polished and processed based on the steps detailed in challenge description[16]. The experiments were carried out on bare plates without any powder using the NIST **A**dditive **M**anufacturing **M**etrology **T**est Bed (AMMT). AMMT has been developed at NIST, and numerous high-quality experiments have been carried out for additive manufacturing process experiments[42–48]. The base laser used for the experiment had a power of 285 W, a scan speed of 960 mm s^-1, and a Gaussian laser spot diameter of 67 µm. In situ and ex situ measurements were recorded using numerous experimental setups that include but is not limited to co-axial melt pool monitoring camera, integrating sphere, and microscopy. These procedures and steps are explained in detail in a report by NIST[16]. In this work, the modeling and prediction of challenge 3, titled AMB2022-03 problems, are discussed in detail.

Computational methods

A finite volume method- (FVM) based C++ code called AM-CFD developed internally at Northwestern University, was used to predict the experimental measurements. The code solved a thermal-fluid model considering liquid flow inside the melt pool driven by the Marangoni effect, as detailed in an earlier work[27], in conjunction with a cylindrical heat source calibration scheme. First, a cylindrical heat source[49] representing the laser heating is implemented in combination with a calibration scheme[40] that initially relies on a reduced-order HOPGD[32,33] model for faster iteration of the calibration data. Then, using an optimized calibration scheme based on initial test runs, the parameters of the cylindrical heat source are calculated. Once the heat source was calibrated, it was capable of estimating heat input to the system for all the laser processing conditions. Based on this calibrated heat source, all the challenge 3 cases were simulated, and the measurements and predictions were made.

Thermal-fluid process model

A transient three-dimensional thermal-fluid model was used to predict the temperature and velocity of the melt pool region. The governing equations include the Navier-Stokes equation in addition to the energy equation, for which the governing equations were as follows:

$$\frac{\partial \rho}{\partial t} + \nabla \cdot (\rho \mathbf{v}) = 0 \tag{1}$$

$$\frac{\partial (\rho \mathbf{v})}{\partial t} + \nabla \cdot (\rho \mathbf{v}\mathbf{v}) = -\nabla P + \mu \nabla^2 \mathbf{v} + \rho \mathbf{g} - \rho \mathbf{g} \beta (T - T_{ref}) + \mathbf{S_m} \tag{2}$$

$$\frac{\partial (\rho H)}{\partial t} + \nabla \cdot (\rho \mathbf{v} \mathrm{H}) = \nabla \cdot (k \nabla \mathrm{T}) + S_\mathrm{h} \tag{3}$$

In the equations above, t is the time, ρ is the density, v is the velocity, P is the pressure, μ is the viscosity, $\boldsymbol{g}$ is the acceleration of the gravity, β is the thermal expansion coefficient, T is the temperature, k is the thermal conductivity, H is the specific enthalpy, S_m is the momentum due to mushy zone resistance, S_h is the total volumetric heat generation or sink of the system. The boundary condition for momentum equation (Eq. (2)) at the top surface is provided as

$$\begin{aligned} \mu \tfrac{\partial v_1}{\partial z} &= f_\mathrm{l} \tfrac{dy}{dT} \tfrac{\partial T}{\partial x} \\ \mu \tfrac{\partial v_2}{\partial z} &= f_\mathrm{l} \tfrac{dy}{dT} \tfrac{\partial T}{\partial y} \\ v_3 &= 0 \end{aligned} \tag{4}$$

Here γ is the surface tension, $\frac{dy}{dT}$ is the Marangoni coefficient, and v_i is the ith component of the velocity.

The surface heat loss or generation included heat loss due to radiation, convection, and evaporation and was employed as a free surface for boundary conditions which in equation form can be related as

$$(k \nabla \mathrm{T}) \cdot \boldsymbol{n} + S_{\mathrm{h,radiation}} + S_{\mathrm{h,convection}} + S_{\mathrm{h,evaporation}} = 0 \tag{5}$$

$S_{h,radiation}$ is the heat loss due to radiation, $S_{h,convection}$ is the heat loss due to convection, and $S_{h,evaporation}$ is the heat loss due to evaporation. The equation relating the enthalpy with temperature is

$$H = h + \Delta H = \int_0^T C_\mathrm{p} dT + \rho L_\mathrm{f} f_\mathrm{l} \tag{6}$$

In the equation, h is sensible heat that is estimated as $\int_0^T C_p dT$ where C_p is the temperature-dependent specific heat capacity. ΔH is the total enthalpy change due to temperature and phase change. The amount of enthalpy change due to phase change is estimated as $\rho L_f f_l$ where L_f is the latent enthalpy of fusion, and f_l is the volume fraction of the liquid phase.

The momentum due to mushy zone resistance S_m is estimated as

$$\boldsymbol{S_\mathrm{m}} = -\frac{180\mu}{\delta_\mathrm{c}^2} \left[\frac{(1 - f_\mathrm{l})^2}{f_\mathrm{l}^3 + B} \right] \boldsymbol{v} \tag{7}$$

In the equation, δ_c is the approximate primary dendritic spacing and set to 1 µm. B is a small parameter to avoid division by zero and is subsequently set to 10^{-3}. The heat loss due to radiation, convection, and evaporation is estimated with the following

equation sets as

$$S_{h,radiation} = \sigma\varepsilon\left(T^4 - T_{\infty}^4\right) \quad (8)$$

Where σ is the Stephan-Boltzman constant, ε is the emissivity, and T_{∞} is the ambient temperature.

$$S_{h,convection} = h_c(T - T_{\infty}) \quad (9)$$

h_c is the heat convection coefficient,

$$S_{\mathrm{h,evaporation}} = \varphi L_{\mathrm{v}}(T) P_{\mathrm{atm}} \sqrt{\frac{m_{\mathrm{A}}}{2\pi k_{\mathrm{B}} T}} e^{\frac{L_{\mathrm{v}}(0) m_{\mathrm{A}}\left(T - T_{\mathrm{b}}\right)}{k_{\mathrm{B}} T T_{\mathrm{b}}}} \quad (10)$$

In this equation, L_v is the latent heat of vaporization, m_A is the atomic mass, k_B is the Boltzmann constant, T_b is the boiling temperature, P_{atm} is the atmospheric pressure, and φ is the evaporation coefficient. For laser heating, φ depends on the vapor Mach number M at the edge of the Knudsen zone, which varies approximately as $0.82\sqrt{M}$. For a vacuum process like Electron Beam Melting (EBM), the value of φ is 0.82[50].

The melt pool region is defined from the temperature contour based on the solidus (T_s) and liquidus temperature (T_l). The liquid volume fraction is estimated based on the following equation

$$f_l = \theta(T - T_s) \cdot \left(1 - \theta\left(\frac{T - T_s}{T_L - T_s}\right)\right) + \theta(T - T_l) \quad (11)$$

In the equation above, θ is the Heaviside step function. Thus, from the equation above, the region of the melt pool is defined as the region where $f_l > 0$.

Adaptive meshing

The developed AM-CFD program has adaptive control of the mesh, which follows a power law as described below:

$$x_{i+1} = x_i + \Delta x \cdot r^{i-1}$$
$$where\, \Delta x = \frac{L}{\sum_{i=1}^{n} r^{n-1}} \quad (12)$$

In the equation, L and n are the length of the sub-domain and the number of control volumes along the x-coordinate. r is the bias ratio that defines how the next control volume dimension is changing. x_{i+1} is the coordinate of the next control volume for a given initial coordinate of a control volume x_i for sub-domain of length L. Given a bias ratio value greater than 1, the meshes are biased towards the lower coordinate location, and for bias ratio values smaller than 1, the meshes are biased towards the higher coordinate locations. The control volume sizes are uniformly distributed for a bias ratio value of 1. In the AM-CFD program, a subdomain of higher resolution is assigned to capture the details of the melt pool information. This higher resolution zone shifts its spatial location along with the laser movement.

As the mesh change also affects the discretization of the volume from one time step to the next, the zones need to have a means of passing their state variables as the time changes. At this point, the state variable changes are accounted for with a linear interpolation that is defined as

$$a_i^{n+1} = a_i^n + \frac{\left(a_{i+1}^n - a_i^n\right)\left(x_i^{n+1} - x_i^n\right)}{x_{i+1}^n - x_i^n} \quad (13)$$

The equation uses state variables of the zone from the current time steps (n) to transfer them to the next time step (n + 1). The properties are updated before the next step of iteration starts.

Thermo-physical properties of the materials

The NIST AM Bench Challenge 3 used IN718 for the experiment. NIST does not provide thermo-physical properties of any materials for the competition; hence, data were collected from the available literature. The properties of the IN718[51] are primarily compiled from available literature and are summarized in Table 3.

Table 3. Summary of the material property[52].

Property	IN718
Solid density (kg m^{-3})	7734
Liquid density (kg m^{-3})	7578
Solidus temperature (K)	1533
Liquidus temperature (K)	1609
Solid specific heat capacity (J $Kg^{-1}K^{-1}$)	435
Liquid specific heat capacity (J $Kg^{-1}K^{-1}$)	755
Solid thermal conductivity (W $m^{-1}K^{-1}$)	11.4
Liquid thermal conductivity (W $m^{-1}K^{-1}$)	31.3
Latent heat of fusion (kJ $kg^{-1}K^{-1}$)	290
Dynamic viscosity (Pa s)	5.30×10^{-3}
Thermal expansion (K^{-1})	1.3×10^{-5}
Surface tension (N m^{-1})	1.8
Marangoni coefficient (N $m^{-1}K^{-1}$)	-3.7×10^{-4}

Calibration of the heat source model

Appropriate modeling of the laser heating source was the key to achieving an accurate prediction for the laser powder bed fusion process. There were different approaches to simplifying the heat source to estimate the heat input to the system arising from the laser source. Most of the literature commonly uses a moving heat flux where the heat source's location changes with time as a representation of the laser scan speed[52,53]. An alternate approach to model the laser heating is the use of a volumetric heat source[27,40,54,55] that can be successfully calibrated to match the melt pool dimensions. A further improved volumetric heat source that considers optical penetration depth can also be considered[56,57]. Ray-tracing-based[58–60] laser heat sources were the most physics-based heat source models where the reflection of the laser from the surface was considered through Fresnel absorption. A comprehensive analysis of different heat source models was carried out by Zhang et al.[49]. However, in this article, a cylindrical heat source was considered for the case of simplicity. The depth of the heat source model is a representation of the optical penetration depth (OPD). Based on literature study, it is concluded that the OPD is defined as the depth where the intensity of the laser energy reduces to $\left(\frac{1}{e} \approx 37\%\right)$[23,61]. However, in our analysis, we have adjusted the depth to approximate the heat input at larger depth for cases operating in keyhole mode. Thus, the model is capable of approximating the melt pool depth at higher accuracy even when surface evolution required for keyhole modeling is not introduced in the computational model. Improving the model prediction with such a heat source requires calibration to accurately represent the heating from the laser source where identification of the calibration parameter was required. Identification of unknown parameters in the laser heat source model employed the HOPGD-based surrogate modeling approach with significantly low computational cost compared to conventional identification approaches such as genetic algorithm[23]. The process was utilized to parameterize the cylindrical heat source for a similar problem[50], with details elaborated in[31,33] and a summary in Supplementary Methods 5. The advantage of using this method was the reduced computational cost with minimal sacrifice in accuracy. The spot radius (r_b), scan speed (V), and power (P) were given as process conditions when modeling the laser heat source. However, due to the evolving surface of the

melt pool and keyhole, along with the vaporized metal in the environment, not all the laser power was absorbed by the materials. Hence, an absorptivity parameter η was introduced to account for the fraction of energy going into the system. Moreover, the variation in laser power, scan speed, and spot diameter affects the vapor-induced depression (keyhole) zone. NIST considered the Gaussian distribution of laser intensity for a given spot diameter of the laser and had chosen the second-moment width for the beam diameter definition, which results in $\sigma = \frac{D}{4}$. The beam diameter was estimated to be four times the standard deviation of the marginal distribution. The current approach assumes a simplified relationship between the volumetric energy density $\left(\frac{P}{V\sigma^2}\right)$ and the characteristic cylindrical domain of the heat source using unknown parameters that must be calibrated.

$$VED_\sigma = \psi = \frac{P}{V\sigma^2} \tag{14}$$

In this article, we introduced three source term parameterization schemes for the optimal calibration of experimental data. Details of these three different parameterization schemes were titled heuristic heat source parameterization, Scaling Law-Based Heat Source Parameterization, and Physics Guided Heat Source parameterization subsequently and is discussed in details in Supplementary Method 1 and 2.

Heuristic heat source parameterization

The heat source model parameters considered for this scheme were

$$d = p_1 \frac{P}{V\sigma^2} RHF^2 \tag{15}$$

$$\eta = \max\left(p_2 \frac{P}{V\sigma^2} RHF^2, 0.28\right) \tag{16}$$

$$r_b = p_3 \frac{P}{V\sigma^2} RHF^2 \tag{17}$$

In the above equations, d, η, and r_b are the depth of the heat source, laser absorptivity, and laser beam radius. P, V, and RHF are the laser power, scan speed, and residual heat factor. The volumetric laser heat source term utilizing these parameters is

$$S_{\text{h,laser}} = \begin{cases} \frac{2P\eta}{\pi r_b^2 d} e^{-\frac{2(x^2+y^2)}{r_b^2}} & z_{top} - z \le d \\ 0 & z_{top} - z > d \end{cases} \tag{18}$$

In this equation, x and y give the spatial location of the center of the cylindrical source region. The source term has a Gaussian distribution in the radial direction. The residual heat factor was first ever demonstrated by Yeung et al.[46] and defined at a specific point as

$$RHF_i = \sum_{k \in S_i} \left(\frac{R - d_{ik}}{R}\right)^2 \left(\frac{T - t_{ik}}{T}\right) L_k \tag{19}$$

The equation defines the RHF by the preheating on point i by a previously scanned point k given by the distance between as d_{ik}, elapsed time t_{ik}, and threshold values R and T, which are 0.2×10^{-3} m and 2×10^{-3} s, respectively, in this analysis for the multi-track or pad cases. For single-track laser scan cases, the RHF takes a value of unity. The coefficients p_1, p_2, and p_3 appearing in Eqs. (15), (16), and (17) are the independent unknowns calibrated using the HOPGD method or PGD for short. The initial guess of these unknowns is chosen at random in a n-D space. The goal of the optimization problem is to minimize an error function defined by the selected criteria. In this case, the objective is to minimize

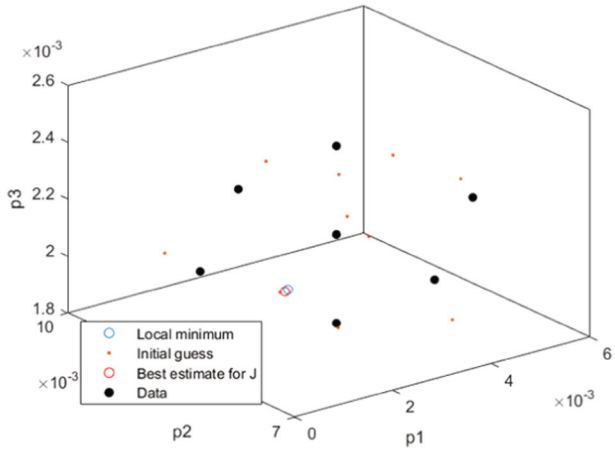

Fig. 14 Representative parameter calibration for the heat source based on literature data for IN718.

the difference between the melt pool width and depth. Assuming the parameter space $\boldsymbol{p} = [p_1, p_2, p_3]$ (Fig. 14) belonging to a predefined domain $\Omega = \Omega_1 \times \Omega_2 \times \ldots \times \Omega_n$, the objective is to minimize the error as defined in the equation

$$\boldsymbol{p}^* = \underset{\boldsymbol{p}\Omega}{\arg\min} \left[J\left(W^{PGD}, W^e, \boldsymbol{p}\right) + J\left(D^{PGD}, D^e, \boldsymbol{p}\right)\right] \tag{20}$$

where W^e and D^e are the experimental width and depth of the melt pool, and J is the objective function that measures the distance between the experimental measurements and reduced order modeling predictions using HOPGD method. The objective function J is defined as

$$J = \sum_{i=1}^{n} w_i ||W_i^{PGD}(p_1, p_2, p_3) - W_i^e|| + \sum_{i=1}^{n} \widetilde{w}_i ||D_i^{PGD}(p_1, p_2, p_3) - D_i^e|| \tag{21}$$

In the equation, the weight coefficient w_i has the property of $\sum_i w_i = 1$, meaning the weight coefficients go down as the deviation increases between experimental and HOPGD prediction measurements.

This calibrated heat source scheme was then used inside the FVM solver to predict the melt pool width, height, cooling rate, and time above melting. However, when the energy density of the laser starts to increase, the deviation from the melt pool measurements starts to increase, which necessitates the improvement of the parameterization scheme.

Scaling law-based heat source parameterization

Based on a recent study[34] proposing that the keyhole aspect ratio depends on a newly discovered dimensionless parameter, the keyhole number (Ke), a parameterization scheme was proposed to predict experiment cases when there was an active formation of keyhole.

The keyhole number Ke is defined as

$$Ke = \frac{\eta P}{(T_l - T_0)\pi\rho C_p \sqrt{\alpha V r_0^3}} \tag{22}$$

In this equation, C_p is the heat capacity, T_l is the liquidus temperature, T_0 is the ambient temperature. This calibration scheme improves the prediction when the keyhole is present; however, at low energy density, the calibration scheme related to the volumetric energy density performs better than this scaling law-based scheme. The parameterization of the heat source is

Table 4. Summary of the cylindrical heat source calibration schemes.

	Heuristic calibration	Scaling law-based calibration	Physics guided calibration
Heat source depth	$d = p_1 \frac{P}{V\sigma^2} RHF^2$	$d = p_1(Ke(p_2) - 1.4)$	$d = p_1 \frac{P}{V\sigma^2} RHF^2$
Heat source energy	$\eta = \max\left(p_2 \frac{P}{V\sigma^2} RHF^2, 0.28\right)$	$\eta = \max\{0.7\left[1 - e^{-0.6Ke(p_2)L_d^*}\right], p_2\}$	$\eta = \max\left(p_2 \frac{P}{V\sigma^2}, 1\right)$
Heat source radius	$r_b = p_3 \frac{P}{V\sigma^2} RHF^2$	$r_b = p_3 L_d^* r_0$	$r_b = p_3 \left(\frac{P}{V\sigma^2}\right)^2 RHF^2$

established by the following equations that are described in[34].

$$d = p_1(Ke(p_2) - 1.4) \tag{23}$$

$$\eta = \max\{0.7\left[1 - e^{-0.6Ke(p_2)L_d^*}\right], p_2\} \tag{24}$$

$$r_b = p_3 L_d^* r_0 \tag{25}$$

In the equations above, the parameters to be calibrated are (p_1, p_2 and p_3), L_d^* is the normalized diffusion length and is quantified as $L_d^* = \frac{\delta_z}{r_0}$ where δ_z is the thermal diffusion length and is related by $\delta_z = \sqrt{\frac{\alpha r_0}{V}}$. In the thermal diffusion length estimate, α is the thermal diffusivity and r_0 is the given laser spot radius. This parameterization scheme was limited in its ability to predict scenarios where there is no keyhole, or the formation of a keyhole is in transition. From the experimental observations, it was found that there is a strong correlation between (VED_σ) and melt pool geometric shapes irrespective of keyhole formation, and this was the basis for the physics-guided heat source parameterization.

Physics guided heat source parameterization

In this parameterization scheme, the volumetric energy density was related to the cylindrical heat source's depth, aspect ratio and the volumetric heat generation (Supplementary Methods 4). Considering the NIST choice of volumetric energy density that established a more accurate scaling relationship between the VED_σ and laser parameters, a new relationship is defined as follows

$$d = p_1 \frac{P}{V\sigma^2} RHF^2 \tag{26}$$

$$\eta = \max\left(p_2 \frac{P}{V\sigma^2}, 1\right) \tag{27}$$

$$r_b = p_3 \left(\frac{P}{V\sigma^2}\right)^2 RHF^2 \tag{28}$$

This new modification improved the prediction of the melt pool geometry at higher VED.

The different heat source calibration schemes are summarized in Table 4.

DATA AVAILABILITY

All computational modeling data relevant to this article is made available through github: https://github.com/neoceph/physics_guided_heat_source. All the experimental data, as made available by NIST, are available here: https://www.nist.gov/ambench/am-bench-2022-challenge-problems-and-measurement-results.

CODE AVAILABILITY

A Finite Volume Method based CFD solver is developed in C++ to run the simulation. The codes that support the findings of this study are available upon reasonable request.

Received: 9 February 2023; Accepted: 3 January 2024;
Published online: 19 February 2024

REFERENCES

1. Ngo, T. D., Kashani, A., Imbalzano, G., Nguyen, K. T. Q. & Hui, D. Additive manufacturing (3D printing): A review of materials, methods, applications and challenges. *Compos. Part B Eng.* **143**, 172–196 (2018).
2. Keller, T. et al. Application of finite element, phase-field, and CALPHAD-based methods to additive manufacturing of Ni-based superalloys. *Acta Mater.* **139**, 244–253 (2017).
3. DebRoy, T. et al. Additive manufacturing of metallic components–process, structure and properties. *Prog. Mater. Sci.* **92**, 112–224 (2018).
4. Yap, C. Y. et al. Review of selective laser melting: Materials and applications. *Appl. Phys. Rev.* **2**, 041101 (2015).
5. Frazier, W. E. Metal additive manufacturing: A review. *J. Mater. Eng. Perform.* **23**, 1917–1928 (2014).
6. Hyer, H. et al. Composition-dependent solidification cracking of aluminum-silicon alloys during laser powder bed fusion. *Acta Mater.* **208**, 116698 (2021).
7. Geng, S., Yang, W., Jiang, P., Han, C. & Ren, L. Numerical study of keyhole dynamics and porosity formation during high-power oscillating laser welding of medium-thick aluminum alloy plates. *Int. J. Heat. Mass Transf.* **194**, 123084 (2022).
8. Promoppatum, P. et al. Quantification and prediction of lack-of-fusion porosity in the high porosity regime during laser powder bed fusion of Ti-6Al-4V. *J. Mater. Process. Technol.* **300**, 117426 (2022).
9. Yang, T. et al. Effect of processing parameters on overhanging surface roughness during laser powder bed fusion of AlSi10Mg. *J. Manuf. Process.* **61**, 440–453 (2021).
10. Feng, S., Kamat, A. M., Sabooni, S. & Pei, Y. Experimental and numerical investigation of the origin of surface roughness in laser powder bed fused overhang regions. *Virtual Phys. Prototyp.* **16**, S66–S84 (2021).
11. Li, L., Li, J-Q. & Fan, T-H. Phase-field modeling of wetting and balling dynamics in powder bed fusion process. *Phys. Fluids* **33**, 042116 (2021).
12. Gasper, A. N. D. et al. Oxide and spatter powder formation during laser powder bed fusion of Hastelloy X. *Powder Technol.* **354**, 333–337 (2019).
13. Sanaei, N. & Fatemi, A. Defects in additive manufactured metals and their effect on fatigue performance: A state-of-the-art review. *Prog. Mater. Sci.* **117**, 100724 (2021).
14. Additive Manufacturing Benchmarks 2018: Home. https://www.tms.org/portal/MEETINGS___EVENTS/TMS_Meetings___Events/Upcoming_TMS_Meetings/AMBench2018/portal/Meetings___Events/2018/AMBench2018/default.aspx?hkey=d2c9f6b8-c4c8-41c4-ac40-63a74911f9ff.
15. CHALLENGE RESULTS ANNOUNCED. *Air Force Research Laboratory (AFRL) Additive Manufacturing (AM) Modeling Challenge Series.* https://materials-data-facility.github.io/MID3AS-AM-Challenge/.
16. AMBench, N. *AMB2022-03 Benchmark Measurements and Challenge Problems.* https://www.nist.gov/document/amb2022-03-measurement-and-challenge-descriptions-version-101 (2022).
17. Simonds, B. J. et al. Simultaneous high-speed x-ray transmission imaging and absolute dynamic absorptance measurements during high-power laser-metal processing. *Procedia CIRP.* **94**, 775–779 (2020).
18. Lane, B. et al. Design, developments, and results from the NIST additive manufacturing metrology testbed (AMMT). in *2016 International Solid Freeform Fabrication Symposium* (University of Texas at Austin, 2016).
19. Vlasea, M. L., Lane, B., Lopez, F., Mekhontsev, S. & Donmez, A. Development of powder bed fusion additive manufacturing test bed for enhanced real-time process control. in *2015 International Solid Freeform Fabrication Symposium* (University of Texas at Austin, 2015).
20. Turner, J. A. et al. ExaAM: Metal additive manufacturing simulation at the fidelity of the microstructure. *Int. J. High. Perform. Comput. Appl.* **36**, 13–39 (2022).
21. Huang, H., Ma, N., Chen, J., Feng, Z. & Murakawa, H. Toward large-scale simulation of residual stress and distortion in wire and arc additive manufacturing. *Addit. Manuf.* **34**, 101248 (2020).

22. Bruna-Rosso, C., Demir, A. G. & Previtali, B. Selective laser melting finite element modeling: Validation with high-speed imaging and lack of fusion defects prediction. *Mater. Des.* **156**, 143–153 (2018).
23. Tran, H.-C. & Lo, Y.-L. Heat transfer simulations of selective laser melting process based on volumetric heat source with powder size consideration. *J. Mater. Process. Technol.* **255**, 411–425 (2018).
24. Ladani, L., Romano, J., Brindley, W. & Burlatsky, S. Effective liquid conductivity for improved simulation of thermal transport in laser beam melting powder bed technology. *Addit. Manuf.* **14**, 13–23 (2017).
25. Robichaud, J., Vincent, T., Schultheis, B. & Chaudhary, A. Integrated computational materials engineering to predict melt-pool dimensions and 3D grain structures for selective laser melting of Inconel 625. *Integrating Mater. Manuf. Innov.* **8**, 305–317 (2019).
26. Chia, H. Y., Wang, L. & Yan, W. Influence of oxygen content on melt pool dynamics in metal additive manufacturing: High-fidelity modeling with experimental validation. *Acta Mater.* **249**, 118824 (2023).
27. Gan, Z. et al. Benchmark study of thermal behavior, surface topography, and dendritic microstructure in selective laser melting of Inconel 625. *Integrating Mater. Manuf. Innov.* **8**, 178–193 (2019).
28. Cunningham, R. et al. Keyhole threshold and morphology in laser melting revealed by ultrahigh-speed x-ray imaging. *Science* **363**, 849–852 (2019).
29. Reijonen, J., Revuelta, A., Riipinen, T., Ruusuvuori, K. & Puukko, P. On the effect of shielding gas flow on porosity and melt pool geometry in laser powder bed fusion additive manufacturing. *Addit. Manuf.* **32**, 101030 (2020).
30. Mollamahmutoglu, M. & Yilmaz, O. Volumetric heat source model for laser-based powder bed fusion process in additive manufacturing. *Therm. Sci. Eng. Prog.* **25**, 101021 (2021).
31. Lu, Y., Jones, K. K., Gan, Z. & Liu, W. K. Adaptive hyper reduction for additive manufacturing thermal fluid analysis. *Comput. Methods Appl. Mech. Eng.* **372**, 113312 (2020).
32. Lu, Y., Blal, N. & Gravouil, A. Adaptive sparse grid based HOPGD: Toward a nonintrusive strategy for constructing space-time welding computational vademecum. *Int. J. Numer. Methods Eng.* **114**, 1438–1461 (2018).
33. Lu, Y., Blal, N. & Gravouil, A. Datadriven HOPGD based computational vademecum for welding parameter identification. *Comput. Mech.* **64**, 47–62 (2019).
34. Gan, Z. et al. Universal scaling laws of keyhole stability and porosity in 3D printing of metals. *Nat. Commun.* **12**, 2379 (2021).
35. Balbaa, M., Mekhiel, S., Elbestawi, M. & McIsaac, J. On selective laser melting of Inconel 718: Densification, surface roughness, and residual stresses. *Mater. Des.* **193**, 108818 (2020).
36. Khorasani, M. et al. A comprehensive study on meltpool depth in laser-based powder bed fusion of Inconel 718. *Int. J. Adv. Manuf. Technol.* **120**, 2345–2362 (2022).
37. Romano, J., Ladani, L. & Sadowski, M. Laser additive melting and solidification of Inconel 718: Finite element simulation and experiment. *JOM* **68**, 967–977 (2016).
38. Sadowski, M., Ladani, L., Brindley, W. & Romano, J. Optimizing quality of additively manufactured Inconel 718 using powder bed laser melting process. *Addit. Manuf.* **11**, 60–70 (2016).
39. Scime, L. & Beuth, J. Melt pool geometry and morphology variability for the Inconel 718 alloy in a laser powder bed fusion additive manufacturing process. *Addit. Manuf.* **29**, 100830 (2019).
40. Gan, Z., Jones, K. K., Lu, Y. & Liu, W. K. Benchmark study of melted track geometries in laser powder bed fusion of Inconel 625. *Integrating Mater. Manuf. Innov.* (2021) https://doi.org/10.1007/s40192-021-00209-4.
41. Kiss, A. M. et al. Laser-induced keyhole defect dynamics during metal additive manufacturing. *Adv. Eng. Mater.* **21**, 1900455 (2019).
42. Yeung, H., Lane, B. M., Donmez, M. A., Fox, J. C. & Neira, J. Implementation of advanced laser control strategies for powder bed fusion systems. *Procedia Manuf.* **26**, 871–879 (2018).
43. Yang, Z., Lu, Y., Yeung, H. & Krishnamurty, S. Investigation of Deep Learning for Real-Time Melt Pool Classification in Additive Manufacturing. in *2019 IEEE 15th International Conference on Automation Science and Engineering (CASE)* 640–647 (2019).
44. Yang, Z., Lu, Y., Yeung, H. & Krishnamurty, S. From scan strategy to melt pool prediction: A neighboring-effect modeling method. *J. Comput. Inf. Sci. Eng.* **20**, 051001–1–051001–12 (2020).
45. Yeung, H., Lane, B. & Fox, J. Part geometry and conduction-based laser power control for powder bed fusion additive manufacturing. *Addit. Manuf.* **30**, 100844 (2019).
46. Yeung, H. & Lane, B. A residual heat compensation based scan strategy for powder bed fusion additive manufacturing. *Manuf. Lett.* **25**, 56–59 (2020).
47. Yeung, H., Yang, Z. & Yan, L. A meltpool prediction based scan strategy for powder bed fusion additive manufacturing. *Addit. Manuf.* **35**, 101383 (2020).
48. Lane, B. et al. Transient laser energy absorption, co-axial melt pool monitoring, and relationship to melt pool morphology. *Addit. Manuf.* **36**, 101504 (2020).
49. Zhang, Z. et al. 3-Dimensional heat transfer modeling for laser powder-bed fusion additive manufacturing with volumetric heat sources based on varied thermal conductivity and absorptivity. *Opt. Laser Technol.* **109**, 297–312 (2019).
50. Cook, P. S. & Murphy, A. B. Simulation of melt pool behaviour during additive manufacturing: Underlying physics and progress. *Addit. Manuf.* **31**, 100909 (2020).
51. Wolff, S. J. et al. Experimentally validated predictions of thermal history and microhardness in laser-deposited Inconel 718 on carbon steel. *Addit. Manuf.* **27**, 540–551 (2019).
52. Lee, Y. S. & Zhang, W. Modeling of heat transfer, fluid flow and solidification microstructure of nickel-base superalloy fabricated by laser powder bed fusion. *Addit. Manuf.* **12**, 178–188 (2016).
53. Zhang, Y. & Zhang, J. Modeling of solidification microstructure evolution in laser powder bed fusion fabricated 316L stainless steel using combined computational fluid dynamics and cellular automata. *Addit. Manuf.* **28**, 750–765 (2019).
54. Xia, M. et al. Influence of hatch spacing on heat and mass transfer, thermodynamics and laser processability during additive manufacturing of Inconel 718 alloy. *Int. J. Mach. Tools Manuf.* **109**, 147–157 (2016).
55. Zhang, D. et al. Thermofluid field of molten pool and its effects during selective laser melting (SLM) of Inconel 718 alloy. *Addit. Manuf.* **21**, 567–578 (2018).
56. Panwisawas, C. et al. On the role of thermal fluid dynamics into the evolution of porosity during selective laser melting. *Scr. Mater.* **105**, 14–17 (2015).
57. Qiu, C. et al. On the role of melt flow into the surface structure and porosity development during selective laser melting. *Acta Mater.* **96**, 72–79 (2015).
58. Wang, L., Zhang, Y., Chia, H. Y. & Yan, W. Mechanism of keyhole pore formation in metal additive manufacturing. *Npj Comput. Mater.* **8**, 22 (2022).
59. Bayat, M. et al. Keyhole-induced porosities in Laser-based Powder Bed Fusion (L-PBF) of Ti6Al4V: High-fidelity modelling and experimental validation. *Addit. Manuf.* **30**, 100835 (2019).
60. Allen, T. R. et al. Energy-coupling mechanisms revealed through simultaneous keyhole depth and absorptance measurements during laser-metal processing. *Phys. Rev. Appl.* **13**, 064070 (2020).
61. Foroozmehr, A., Badrossamay, M., Foroozmehr, E. & Golabi, S. Finite element simulation of selective laser melting process considering optical penetration depth of laser in powder bed. *Mater. Des.* **89**, 255–263 (2016).

ACKNOWLEDGEMENTS

We acknowledge the NIST AM Bench organizing committee for their high-quality experimental datasets and the United States National Science Foundation (NSF) funding under Grant No. CMMI-1934367 and Center for Hierarchical Material Design (CHiMaD).

AUTHOR CONTRIBUTIONS

A.A.A. analyzed experimental data, developed code, performed simulations, compiled the experimental and simulation data, and drafted the manuscript. Y. Li performed HOPGD simulations, conducted preliminary literature study, and contributed to the manuscript preparations. Y. Lu developed HOPGD code, supervised HOPGD simulations, contributed to the manuscript preparations. X. Xie Conducted preliminary literature study, compiled literature data. Z. Gan Contributed and supervised literature study, data compilation, code development, manuscript preparation. S.M. contributed to manuscript draft and method development, G.W. contributed setting up the simulations, writing draft, and research supervision. W.K.L. supervised the research, led the study, contributed to the analysis, preparation and revision of the manuscript. All authors reviewed and approved the manuscript.

COMPETING INTERESTS

The authors declare no competing interests.

ADDITIONAL INFORMATION

Supplementary information The online version contains supplementary material available at https://doi.org/10.1038/s41524-024-01198-6.

Correspondence and requests for materials should be addressed to Abdullah Al Amin or Wing Kam Liu.